J. Fluid Mech. (1987), *vol.* 184, *pp.* 15–41
Printed in Great Britain

Experiments on ripple instabilities. Part 1. Resonant triads

By DIANE M. HENDERSON† AND JOSEPH L. HAMMACK
Department of Engineering Sciences, University of Florida, Gainesville, FL 32611, USA

(Received 9 July 1986 and in revised form 17 March 1987)

Water waves for which both gravitation and surface tension are important (ripples) exhibit a variety of instabilities. Here, experimental results are presented for ripple wavetrains on deep water with frequencies greater than 19.6 Hz where a continuum of resonant triad interactions are dynamically admissible. The experimental wavetrains are indeed unstable, and the instability becomes more pronounced as nonlinearity is increased. The unstable wavefield is characterized by significant spatial disorder while temporal measurements at fixed spatial locations remain quite ordered. In fact, for most experiments temporal measurements suggest that a selection process exists in which a single triad dominates evolution. The dominant triad typically does not involve a subharmonic frequency of the generated wave and persists over a wide range of amplitudes for the initial wave. Viscosity does not appear to be important in the selection process; however, it may be responsible for the lack of subsequent triad production by the excited waves of the initial triad. The presence of a selection process contradicts previous conjecture, based on the form of the interaction coefficients, that a broad-banded spectrum of waves should occur. The general absence of subharmonic growth also contradicts previously reported experiments. Results are also presented for wavetrains at the parametric boundary of 19.6 Hz and a degenerate case of resonant triads at 9.8 Hz (Wilton's ripples). In addition to resonant triads, the experiments show evidence of (generally) weaker narrow-band interactions.

1. Introduction

Waves on the ocean surface may be classified according to the restoring forces responsible for their motions. Although classification boundaries are necessarily indistinct, representative values of lengths and frequencies are easily chosen. For example, gravitation g dominates for gravity waves with lengths greater than about 10 cm and frequencies less than about 5 Hz. Surface tension T dominates for capillary waves whose lengths are smaller than about 0.5 cm and whose frequencies exceed about 50 Hz. For the intermediate range in wavelengths of 10–0.5 cm and frequencies of 5–50 Hz, both gravitation and surface tension are important; for brevity, we refer to these gravity–capillary waves as ripples. This paper is the first of two in which the evolution of ripple wavetrains on deep water is examined experimentally. The results are separated into two parts as a consequence of differing ripple dynamics on each side of a distinct frequency boundary at 19.6 Hz for a 'clean' surface. In Part 1 we report results for wavetrains with frequencies greater than 19.6 Hz as well as a special case at 9.8 Hz. Results for ripple wavetrains with frequencies less than 19.6 Hz will be presented in Part 2.

† Present address: Institute of Geophysics and Planetary Physics, University of California, La Jolla, CA 92093, USA.

The periodic wavetrain is of fundamental importance in both the theoretical and experimental study of water waves. As a permanent-form solution of approximate linear theories, it has served since Stokes (1847) as a basic building block for studying the effects of weak nonlinearity. Simple oscillatory waves are also very easy to generate in a laboratory setting. A major factor determining the usefulness of the periodic wavetrain is its stability to perturbations. Unfortunately, ripple wavetrains are fraught with instabilities which occur quickly in the laboratory and at leading-order considerations of nonlinearity in the theoretical models. An important example of leading-order instability is provided by the analysis of Harrison (1909) and Wilton (1915) who show that the ripple wavetrain with wavenumber magnitude

$$k^* = \left(\frac{\rho g}{2T}\right)^{\frac{1}{2}}, \tag{1}$$

is unstable to its second harmonic. (In (1) ρ is the mass density of water.) Using the linear dispersion relation for ripples on water of depth h, radian frequency ω, and wavenumber magnitude k, i.e.

$$\omega^2 = \left(gk + \frac{T}{\rho}k^3\right)\tanh kh, \tag{2}$$

'Wilton's ripples' are found to have a cyclic frequency of $f^* = \omega^*/2\pi = 9.8$ Hz on deep water ($h \rightarrow \infty$) when $T = 73$ dyn/cm. In fact, a countable set of ripples exists given by $k_n^* = (\rho g/nT)^{\frac{1}{2}}, n = 2, 3, \ldots$; each is unstable to its nth harmonic. In addition to the role of Wilton's ripples in the overall understanding of nonlinear wavetrains, their second harmonic with a frequency of $2f^* = 19.6$ Hz corresponds to the parametric boundary in ripple dynamics mentioned above. The special importance of Wilton's ripples and their second harmonic is demonstrated in the study of resonant interactions among ripples.

Many instabilities resulting from weak nonlinearity among water waves can be described in the context of RIT (resonant interaction theory). The fundamental notion of RIT was formulated by Phillips (1960) for gravity waves on deep water. Benney (1962) *inter alios* realized the general nature of its application to dynamical systems. The basic idea is that the effects of weak nonlinearity may be dominated by certain wave–wave interactions which satisfy 'resonance' conditions. At leading order in weak nonlinearity the quadratic interactions of significance occur among three waves whose wavenumber vectors (or simply, wavevectors) $\boldsymbol{k} = (l, m)$ and frequencies ω, as determined by the linear dispersion relation, satisfy the kinematical constraints

$$\left.\begin{aligned} \boldsymbol{k}_1 &= \boldsymbol{k}_2 + \boldsymbol{k}_3, \\ \omega_1 &= \omega_2 + \omega_3. \end{aligned}\right\} \tag{3}$$

If resonant triads are possible then a dynamical analysis yields a set of nonlinear, coupled equations for the spatial and temporal evolution of the complex amplitude for each triad member. For a single triad, there are three equations which are similar for all dynamical systems, differing only in the 'interaction coefficients' among the three waves. If no triads of waves exist which satisfy (3) then cubic interactions at the second order in weak nonlinearity must be considered. Here, resonant quartets are dominant in which the four waves satisfy the kinematical conditions

$$\left.\begin{aligned} \boldsymbol{k}_1 \pm \boldsymbol{k}_2 \pm \boldsymbol{k}_3 \pm \boldsymbol{k}_4 &= 0, \\ \omega_1 \pm \omega_2 \pm \omega_3 \pm \omega_4 &= 0. \end{aligned}\right\} \tag{4}$$

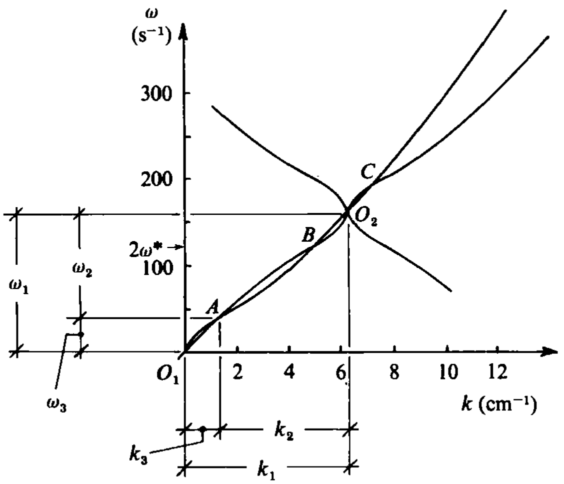

FIGURE 1. Graphical solution of the kinematic resonance condition (after Simmons 1969) for collinear triads among ripples for a 25 Hz test-wave; $h = 4.9$ cm and $T = 73$ dyn/cm.

Both resonant triads and quartets are important in the experimental study of ripples. Even though there is a continuum of ripple triads available, Hasselmann's theorem (1967) shows that they are accessible only in experiments with test-wave frequencies greater than $2f^* = 19.6$ Hz. (Wilton's ripples with a frequency of 9.8 Hz are a degenerate case which experience a resonant triad interaction such that $k_1 = 2k^*$, $k_2 = k_3 = k^*$ and $\omega_1 = 2\omega^*, \omega_2 = \omega_3 = \omega^*$.) For test waves with frequencies less than 19.6 Hz, quartets are the first resonant interactions, and we report experimental results for quartets in Part 2.

The organization of this paper is as follows. Theoretical predictions of RIT for ripple triads are reviewed in §2 with an emphasis on those details which are most pertinent to the experimental study. The laboratory facilities, experimental procedures, and other experimental considerations are described in §3. Both qualitative and quantitative data from the experiments are presented and discussed in §4. Here, we also describe previous experiments of Bannerjee & Korpel (1982) which appear to contradict our results. Our major conclusions regarding resonant triad interactions among ripple wavetrains are reviewed in §5.

2. Theoretical considerations

The kinematic possibility of resonant triads for any dynamical system is most easily determined by a graphical procedure outlined by Simmons (1969) in the context of ripples. Figure 1 (after Simmons 1969) shows the graphical solution of (3) using (2) when the wavevector of each ripple wavetrain in the triad is collinear. The figure is constructed and interpreted as follows. First, the dispersion relation (2) is shown in (ω, k) space with an origin at O_1. In the calculations for figure 1 we have taken $h = 4.9$ cm and $T = 73$ dyn/cm which correspond to experimental values in §4, and, for clarity, only one branch of (2) is presented. Secondly, a point on the dispersion curve corresponding to a test wave is chosen as the origin O_2 for a graph of all branches of the dispersion relation. In figure 1 a test wave with a frequency of 25 Hz is chosen which corresponds to one of our actual experiments. (Here and throughout this paper we identify the test wave as k_1 and ω_1.) The intersection points of the two dispersion curves at A, B, and C, represent the collinear, resonant triads that are possible for the particlar test wave. The individual members of each triad are found easily as shown for the A triad. It is important to note that as the test-wave frequency approaches $2\omega^*$ from above, the A and B intersections approach one another; they coalesce at a test-wave frequency of $2\omega^*$. For test-wave frequencies less than $2\omega^*$ the A and B points disappear so that only one triad at C is possible.

Figure 1 may be generalized to waves with non-collinear wavevectors by rotation of the dispersion curves about the frequency axes. When rotation is performed (see Simmons 1969), the A and B intersections are found to lie on a closed curve providing a continuum of possible triads. The minimum frequency of any wave in this continuum is that of the lowest frequency wave (ω_3, k_3) in the A collinear triad; the maximum frequency in the continuum is $(\omega_1 - \omega_3)$. As for the collinear case, when the frequency of the test wave approaches $2\omega^*$ from above, the closed curve degenerates to a point, and disappears for frequencies less than $2\omega^*$. After rotation the C intersection point of figure 1 is found to lie on an open curve where all available triads in this continuum have at least one member with a frequency exceeding that of the test wave.

The special role of the $2\omega^*$ frequency in the kinematical resonant conditions has important dynamical significance for the experimental study. According to a theorem by Hasselmann (1967), if only one member of a triad is present initially with significant energy, then it must have the highest frequency in order to excite the other two members. Since the test waves are generated directly by the wavemaker and must excite the other triad members which are embedded in the background noise inherent in the tank, Hasselmann's theorem requires the test wave to have the highest frequency. Hence, only triads on the closed-curve continuum are dynamically accessible. (Wilton's ripples with a frequency of 9.8 Hz are an exception to Hasselmann's theorem and a degenerate case of triad resonance.)

The three-wave equations governing the spatial $\boldsymbol{x} = (x, y)$ and temporal t evolution for an isolated, resonant triad for any non-conservative, dynamical system may be written (e.g. see Craik 1986) as

$$(\partial_t + \boldsymbol{U}_i \cdot \nabla) A_i + \delta_i A_i = i\gamma_i A^*_{i+1} A^*_{i+2}, \tag{5}$$

where δ_i are complex decay constants (assumed real herein); A_i are complex amplitudes (with complex conjugate denoted by $*$); $\boldsymbol{U}_i$ are group velocities; γ_i are real interaction coefficients; $\nabla = (\partial_x, \partial_y)$, and $i = 1, 2, 3$ are interchanged cyclically. The interaction coefficients for resonant triads among ripples on deep (inviscid) water are given by Simmons (1969) as

$$\gamma_i = -\frac{k_i}{4\omega_i} \sum_{j=1}^{3} \omega_j \omega_{j+1} (1 + \hat{\boldsymbol{e}}_j \cdot \hat{\boldsymbol{e}}_{j+1}), \tag{6}$$

where $\hat{\boldsymbol{e}}_j = \boldsymbol{k}_j / k_j$, and j is interpreted as modulo 3. The evolution equations for the real amplitudes a_i and real phases ϕ_i follow from (5):

$$\partial_t a_i + \delta_i a_i + \nabla \cdot (\boldsymbol{U}_i a_i) = a_{i+1} a_{i+2} \gamma_i \sin\phi, \tag{7a}$$

$$\partial_t \phi_i + \nabla \cdot (\boldsymbol{U}_i \phi_i) = \frac{a_{i+1} a_{i+2}}{a_i} \gamma_i \cos\phi, \tag{7b}$$

where $\phi = \phi_1 + \phi_2 + \phi_3$. Special solutions of (5) are known (Craik 1986); Simmons (1969) and McGoldrick (1965) discuss special solutions of (7) in the context of ripples for $\delta_i = 0$. However, none of these solutions appear to be relevant for the experiments considered here.

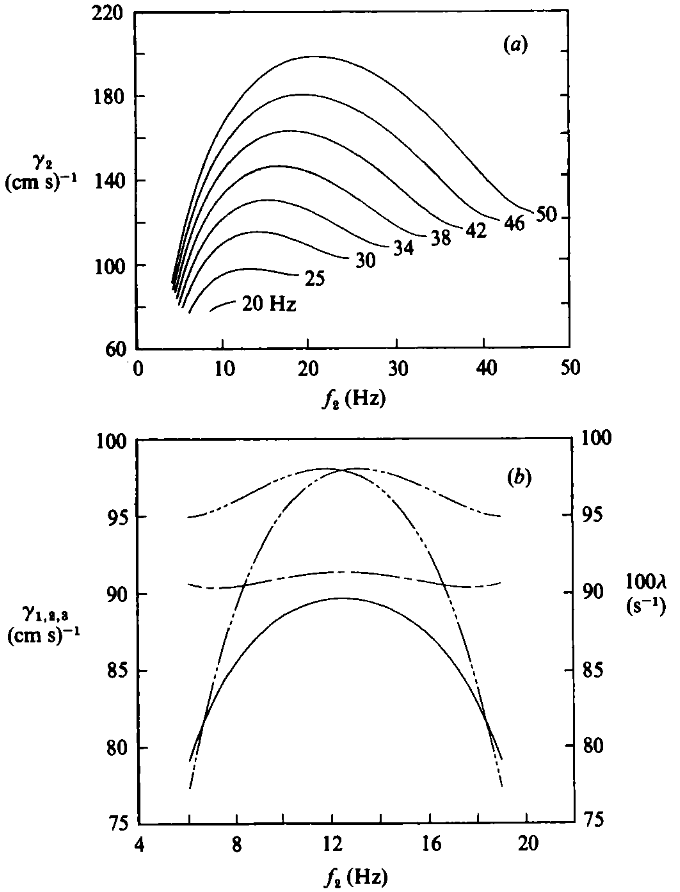

FIGURE 2. Theoretical interaction coefficients for ripple triads with $h = 4.9$ cm and $T = 73$ dyn/cm. (*a*) γ_2 *vs*. f_2 for a series of test-wave frequencies. (*b*) Interaction coefficients and initial growth rate for a 25 Hz test-wave: —-—, $-\gamma_1$; —--—, γ_2; —---—, γ_3; ——, 100λ ($\phi = \frac{1}{2}\pi, a_1 = 0.2$ mm).

An approximate solution of (7) is easily found which does have importance for the experiments. As already noted, one wave is generated directly in the experiments, say $a_1 = O(1)$, whereas the other triad members are quite small initially, say $a_2 \sim a_3 = O(\epsilon)$. Making use of these scalings and neglecting spatial variations, (7) can be linearized to find that the early evolution of the small waves is approximated by

$$\ddot{a}_j + \dot{a}_j(\delta_2 + \delta_3) + a_j(\delta_2 \delta_3 - \gamma_2 \gamma_3 a_1^2 \sin^2 \phi) = 0, \tag{8}$$

where a_1 and ϕ remain at their initial values in this approximation and $j = 2, 3$. The exponential solutions of (8) have a growth–decay rate of

$$\lambda = -\tfrac{1}{2}(\delta_2 + \delta_3) \pm \tfrac{1}{2}((\delta_2 + \delta_3)^2 - 4(\delta_2 \delta_3 - \gamma_2 \gamma_3 a_1^2 \sin^2 \phi))^{\frac{1}{2}}, \tag{9}$$

for the background triad members. Before proceeding it is useful to introduce specific decay constants for waves in the ripple experiments. Henderson & Lee (1986) found that the experimental facilities and procedures to be described in §3 yield water surfaces whose damping characteristics on waves are predicted accurately by the model for an 'inextensible' surface (Lamb 1932, p. 631), i.e.

$$\delta_i = \tfrac{1}{2} k_i (\tfrac{1}{2} \nu \omega_i)^{\frac{1}{2}}, \tag{10}$$

where ν is the kinematic viscosity of water. Using (6) and (10) it is easily shown that $\gamma_i \gg \delta_i$; hence, according to (9), λ is real. Further, a threshold amplitude is required for the background waves to grow initially (i.e. $\lambda > 0$). The threshold amplitude is minimum for $\phi = \frac{1}{2}\pi$ and found from (9) to be

$$a_1 = \left(\frac{\delta_2 \delta_3}{\gamma_2 \gamma_3}\right)^{\frac{1}{2}}. \tag{11}$$

Even though exact solutions of (7) are not available for our experiments, it is reasonable to anticipate that the interaction coefficients γ_i of (6) might provide some insight into selectivity among the continuum of triads available. Figure 2(*a*) shows the interaction coefficient γ_2 as a function of the frequency f_2 for a series of test waves with frequencies 20 Hz $\leqslant f_1 \leqslant$ 50 Hz. The span in frequency f_2 for each of the test-wave frequencies f_1 represents the band of admissible triad frequencies; note that this band widens rapidly as f_1 increases. Results in figure 2 are based on a water depth of $h = 4.9$ cm (effectively the same as $h \rightarrow \infty$) and surface tension $T = 73$ dyn/cm. (These results also correspond to the experiments described in §4.) The initial growth rate λ exhibits a maximum at the subharmonic frequency of the test wave. A near-subharmonic extremum also occurs for the interaction coefficients γ_1, γ_2 and γ_3 as illustrated in figure 2(*b*) for a 25 Hz test wave. In all cases the variation of each coefficient is smooth, exhibiting no strong sensitivity to a single frequency. This lack of sensitivity led Simmons (1969) to conjecture that all waves in the band of admissible frequencies would probably be excited.

3. Experimental programme

The experimental programme is performed in a facility especially designed and constructed to study waves in the ripple regime. Relative to gravity waves, ripples are substantially more difficult to study experimentally. These difficulties have been noted by a number of experimentalists beginning with Rayleigh (1890). Difficulties arise primarily from two sources: (i) resolution of the very small wave amplitudes necessary to study weak nonlinearity in an inherently noisy world, and more importantly, (ii) the complicated nature of contamination effects on a real and straining water surface. Below we describe the equipment, procedures, and other considerations involved in coping with these experimental difficulties. Due to the present lack of a theoretical basis for some experimental observations and the general sensitivity of ripple experiments to extraneous effects, considerable detail is presented in the discussion of facilities and procedures.

3.1. *Equipment and procedures*

The laboratory equipment is conveniently divided into five groups: the wave tank and instrument-positioning system, the wave generator and associated electronics, the water-supply system, the computer system, and the wave gauge. All of the equipment is housed in a ground-floor room isolated from most pedestrian traffic and other building activities.

The wave tank consists of a basin 91 cm wide, 183 cm long, and 15 cm deep, constructed of 1.27 cm tempered glass inset into an aluminium frame. The tank is sealed against leakage with aquarium silicone and supported on a welded-steel frame by adjustable studs which permit precise levelling. The entire tank assembly is supported on the laboratory floor by vibration-isolation pads. Precision ground, case-hardened stainless-steel rods are mounted on the top flanges of the basin sidewalls and levelled with respect to a quiescent water surface. These rails support an instrument carriage which moves on Thompson linear ball bushings. The carriage has similar rails on which instrumentation platforms move in a similar manner. Hurst Model LAS stepper motors allow precise and smooth XY positioning of the instrumentation platforms over the basin. A polyethylene-covered frame is supported over the tank by a pulley system so that the tank can be covered during experiments. (The cover reduces fall-out contamination of the water surface and wind-induced wave motions.) Temporary sidewalls made of (wetted) aluminium may be set into the basin on each side of the wavemaker paddle to create a test channel 91 cm long. The experiments reported herein are performed both with and without these sidewalls. All components of the tank in contact with water are cleaned with ethyl alcohol before each experiment.

Waves are generated by a (wetted) aluminum paddle with a length of 30.4 cm which is supported over the water surface and oscillated vertically. The paddle is shaped in the form of a slender, right-angled wedge whose sloped face is 1 cm long and makes an angle of 25.8° with the vertical. The paddle is located astride the long axis of the tank at a distance of 31 cm from one endwall. The quiescent water surface intercepts the wedge near its midpoint. The paddle and its actuator are supported on a platform through vibration-isolation pads. This platform is supported by a separate, welded-steel frame shaped as an inverted U over the wave tank, and bolted to the laboratory floor through vibration-isolation pads. The paddle is oscillated vertically by an electrodynamic shaker (Bruel and Kjaer Mini-Shaker Type 4810). The actual paddle motion is monitored by a proximity sensor (Kaman Sciences Model DK-2310) which provides a position-feedback signal to a servo-controller. The servo-controller accepts a command signal, compares it to the feedback signal, and provides an appropriate drive current to the shaker in order for the paddle to follow accurately the command signal. All command signals for the triad experiments are sinusoidal.

A special water-supply system is used for all ripple experiments. The system contains approximately 60 gal. of water stored in two polyethylene crocks which are plumbed to the wave tank and a filtering system by tygon tubing, PVC piping, and PVC valves. The crocks and piping system are sealed; air flow into and out of the system during changing water levels is filtered through glass wool. The water filtering system consists of three Sybron–Barnstead pressure cartridges which remove organics, minerals, and particulate matter larger than 0.2 μm, respectively. A Gorman–Rupp metering pump with polypropylene bellows and connectors is used to provide the low flow rates necessary to optimize filter performance. An inline conductivity meter provides a constant measure of ionic purity. (Unfortunately, ionic purity does not assure a clean surface, since many contaminants are not ionic in nature.) In a typical experiment water from the crocks is gravity fed into the basin. At the completion of experiments the water is pumped through the filtering system and returned to the crocks. The plumbing also allows water to be pumped directly between the crocks through the filtering system. The water-supply system is located in the ripple laboratory so that the temperature (20 °C) of the water remains in equilibrium with that of the room.

A DEC MicroPDP-11 computer system is an integral part of the laboratory facility. With analog input and output capabilities, the computer system supports real-time generation of wavemaker command signals, dynamical calibration of the wave gauge,

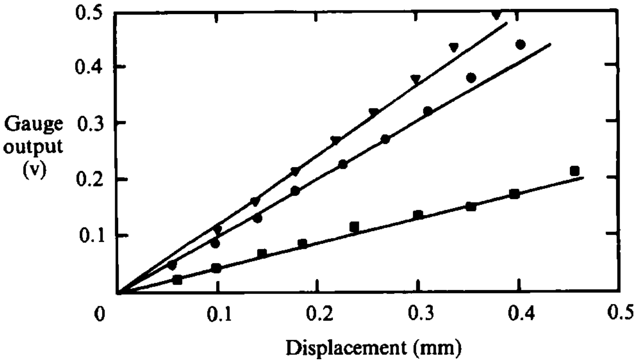

FIGURE 3. Dynamic calibrations of wave gauge. ▼, 10 Hz; ●, 15 Hz; ■, 25 Hz.

collection of wave gauge data, and near real-time data analysis with graphical output. Computer control of experiments has proven indispensable in performing definitive and repeatable experiments in the ripple regime.

Water surface elevations as a function of time at a fixed spatial location are obtained using an *in situ*, high frequency, capacitance-type gauge. The time-varying height of a water column is used to detune a 2 MHz oscillator whose signal is then mixed with a reference frequency to obtain a difference value. Variations in this difference frequency are then transmitted to a frequency-to-voltage converter using a pulsed FM current loop. Power isolation to the gauge is provided by a d.c.–d.c. converter. The gauge output is remarkably free of electrical noise and, while originally developed to measure gravity waves (Howell, private communication), has sufficient sensitivity to measure the ripples reported herein. The water-penetrating portion of the gauge consists of a glass tube, 1.6 mm in outside diameter, which contains a conductor and is sealed at the underwater end. The probe diameter is not negligible compared to the smallest wavelengths (about 6 mm) encountered in the experiments, and necessarily averages the amplitudes of these waves. The use of glass for the dielectric between water and the conductor has proven essential in using an *in situ* gauge. Glass has the property that the static meniscus around the gauge retains its orientation during wave motion; i.e. the meniscus does not flip-flop during reversal of water motion along the gauge. (High-speed video has been used to observe the meniscus orientation for ripples.)

The wave gauge is supported above the water surface by an electrodynamic shaker with a position feedback probe identical to that used with the wavemaker. This arrangement allows dynamic calibrations of the wave gauge to be performed rapidly by the computer. Using the sinusoidal command signal the wave gauge is oscillated at a fixed frequency with varying amplitudes through a quiescent water surface. The gauge output and feedback signals are sampled, and a calibration curve is prepared. The entire process for a ten-point calibration requires about 1 min. Examples of these calibration curves are shown in figure 3 for three frequencies of oscillation. While the gauge output is nearly linear with varying wave amplitudes, it is nonlinearly related to wave frequency, with output decreasing as frequency increases. It is important to note that in the triad experiments of §4 the wavefields will contain more than one distinct wave frequency. In each case we will apply only the calibration curve of the generated wave; hence, the amplitudes of lower-frequency waves will be exaggerated while higher frequencies are attenuated. Only one gauge is available for the experiments.

The wave gauge signal is also conditioned by a Krohn–Hite (Model 3232) two-channel electronic filter before it is recorded. The first channel is used to low-pass the gauge signal and apply a 20 dB amplification to the output. For the triad experiments a cutoff frequency of 100 Hz is set for the low pass. The amplified signal is then high-passed by the second channel at a cutoff frequency of 1 Hz. Another 20 dB amplification of the output is then performed. A Butterworth response for each filter is employed. The primary use of the band-pass process in the triad experiments is to eliminate high-frequency noise that might lead to aliasing in the data analysis and low-frequency noise resulting from building motions and normal-mode oscillations of the water in the tank.

3.2. *Special considerations*

The programme of study on ripples requires experimental results to be reproducible. The major limitations on reproducibility relate to the nature of the water surface and background surface motions (noise) present in the tank. Preliminary experiments using unprepared tap water yielded wildly varying results, contrary to the observations of McGoldrick (1970). The initial use of a third floor laboratory site also proved to be unwieldy; experimental data could be obliterated from vibrations excited by a single person walking down the hallway. While neither of these factors are controlled to complete satisfaction, the present water supply and laboratory site along with other facilities and procedures do permit sufficient reproducibility to obtain definitive results for some aspects of ripple dynamics.

Ripple amplitudes as small as 0.03 mm are encountered in the experiments presented in §4. Reliable measurements of such small amplitudes are difficult to obtain without contamination by background noise in the tank. The major source of background noise is building motion. Efforts to minimize background waves include (i) the use of vibration-isolation mounts on the tank and wavemaker support structures, (ii) the use of a ground-floor room, isolated from pedestrian traffic and building activities, with a concrete slab floor on which the building rests, and (iii) the minimization of movement in the laboratory during an experiment by utilizing computer control of the facility. In addition, all of the experiments reported here were conducted on weekends and nights when building activity was minimum.

In order to provide insight into the signature of background noise present, a periodogram of the wave-gauge signal prior to one experiment is presented in figure 4. The periodogram shows the energy density R^2, in arbitrarily scaled units, as a function of frequency in the range 1–100 Hz. The calculations of figure 4 are based on the Sande–Tukey Radix-2 FFT (fast Fourier transform) which will be used and discussed further in §4. The sampling frequency of 200 Hz and sampling interval of 2.56 s used in obtaining this periodogram corresponds to those used in analysing wave data in §4. The dominant background noise observed occurs at fairly low frequencies, primarily in the gravity-wave regime of less than 5 Hz. (The sampling interval used here does not allow this low-frequency noise to be resolved well.) The low-frequency noise is (presumably) a consequence of building motions and normal-mode oscillations in the tank. There is also consistent noise energy at 60.16 Hz, which corresponds to electrical noise, and 92.19 Hz which results from a mechanical resonance of the wavemaker paddle. Although not present in figure 4, other noise periodograms indicate that significant energy can also appear at 35.16 Hz. It should be emphasized that the display of four decades of energy density R^2 in figure 4 is a consequence of the resolution capability of wave amplitudes. The scaling for R^2 is chosen according to the measured level of background noise prior to an experiment. A single scaling

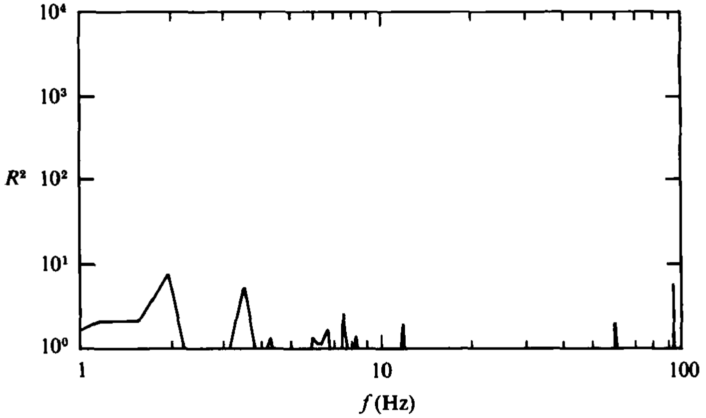

FIGURE 4. Periodogram of background noise.

is chosen for experiments at a fixed test-wave frequency so that the energy density of background noise lies within the lowest decade, such as presented in figure 4. While the noise level is checked before all experiments, its occurrence is unpredictable. There is also evidence that wavemaker motion enhances tank noise, presumably through vibrations of the tank which penetrate the isolation systems. Hence, the noise signature of figure 4 should be recalled when examining periodograms of wave data in §4.

While it is possible to produce perfectly clean water surfaces (Scott, 1979), the necessary measures are too extreme for the volume of water and surface accessibility required for the experiments herein. Contamination invariably occurs which gives rise to surface films. These films cause a general lowering of surface tension in time and have a dramatic effect on the damping of wave motions. (Spatial gradients in tension on a surface unstrained by waves are removed rapidly by the fluid motions they cause.) The tension and damping characteristics of water surfaces utilized in the experiments herein are described by Henderson & Lee (1986). They found that the surface tension always equals the standard handbook value, whether measured by a Du Nouy tensiometer (Fisher Model 20) for a quiescent surface or inferred from (2) using measured wavelengths for a surface strained by small-amplitude waves. This property is reaffirmed by wavelength measurements prior to each experimental series. As noted in §2, Henderson & Lee (1986) also found that wave damping on these surfaces was predicted accurately by the model for an inextensible surface. The notion of an inextensible or 'fully contaminated' surface to account for increased wave damping by films is described by Lamb (1932, p. 631). Essentially, this model places a no-slip boundary condition on the horizontal component of water velocity at the surface. Earlier Lamb (1895, pp. 552–555) as well as more recent authors (e.g. see Lucassen-Reynders & Lucassen 1969) discuss models that also account for spatial gradients in surface tension due to the thickening and thinning of films by waves. These models show that damping at twice the rate of that for an inextensible surface may occur. Based on these models and the measured results by Henderson & Lee, there is no doubt that the water surfaces used herein are contaminated by films. However, gross contamination effects are avoided, and experimental results are reproducible. Both the tension and damping characteristics of the surfaces remain constant during the period of measurements.

4. Experimental results and discussion

Experimental data are presented for ripple wavetrains with input frequencies ranging from 19.6 Hz to 46 Hz and the special case of Wilton's ripples at 9.8 Hz. The water depth $h = 4.9$ cm for all experiments; the measured surface tension $T = 73$ dyn/cm corresponds to the standard handbook value at the laboratory temperature of 20 °C. Quantitative data consist of time series for the water surface elevation η at various positions x downstream and distances y from the centreline of the wavemaker paddle. (The coordinate system is sketched in figure 5a). Each time series is filtered using a pass band of 1–100 Hz prior to being digitized. A sampling interval of 2.56 s is chosen during which 512 equally spaced samples are obtained. A harmonic analysis is then performed using a standard Sande–Tukey Radix FFT (e.g. see Bloomfield 1976, p. 75). Results are presented as periodograms showing the spectral energy density R^2 as a function of the wave frequency f. The sampling interval results in a frequency spacing $\Delta f = 1/2.56 = 0.39$ Hz between FFT calculations of energy density; hence, the results do not allow proper resolution of the energy bandwidth for low-frequency signals. Fortunately, the waves of primary interest here have frequencies (generally much) greater than 5 Hz so that only the resolution of background noise (see §3.2) is impacted seriously. Wave frequencies resolved by the FFT calculations will also be Doppler shifted by any currents in the test channel. (Currents may arise from mass transport by waves, induced streaming at the free surface, and long-wave noise.) The amount of frequency shift is easily detected by comparing the test-wave frequency resolved by the periodogram with the programmed frequency of the wavemaker. Unless otherwise stated, all frequencies quoted in §4 will be those resolved by the periodograms. As noted in §3.2, an arbitrary scaling is chosen for R^2 such that the background noise in the tank prior to a series of experiments lies in the lowest decade of a four-decade presentation. We emphasize that the scaling remains fixed for all data at a single frequency so that relative comparisons are possible within an experimental series.

Most wave data are obtained in a channel of breadth $b = 30.5$ cm formed by placing temporary sidewalls directly adjacent to the wavemaker paddle. Sidewalls are used to confine the energy of the evolving wavefield, thus enhancing wave amplitudes and their resolution. Of course, the sidewalls change the continuum of possible triads on an infinite water surface into a countable set. Data are also presented without the temporary sidewalls where the full tank width of 91 cm allows a denser set of possible triad modes.

Quantitative data are presented first for 25 Hz test-waves where the stroke of the wavemaker paddle is increased until cross-waves evolve and break near the paddle. Qualitative data are also presented for these wavetrains in the form of overhead photographs of the water surface. The photographs show patterns of wave evolution typical of those observed in all experiments. After a fairly extensive discussion of the 25 Hz wavetrains, data are presented and discussed briefly for other test-wave frequencies including the parametric boundary at 19.6 Hz and Wilton's ripples at 9.8 Hz. These results are followed by a discussion of cross waves and the previous experimental results of Bannerjee & Korpel (1982).

4.1. *The 25 Hz wavetrain*

4.1.1. *Spatial data*

In order to illustrate the overall evolution of ripple wavetrains from generation to near extinction by viscosity, spatial views of six different 25 Hz wavetrains are

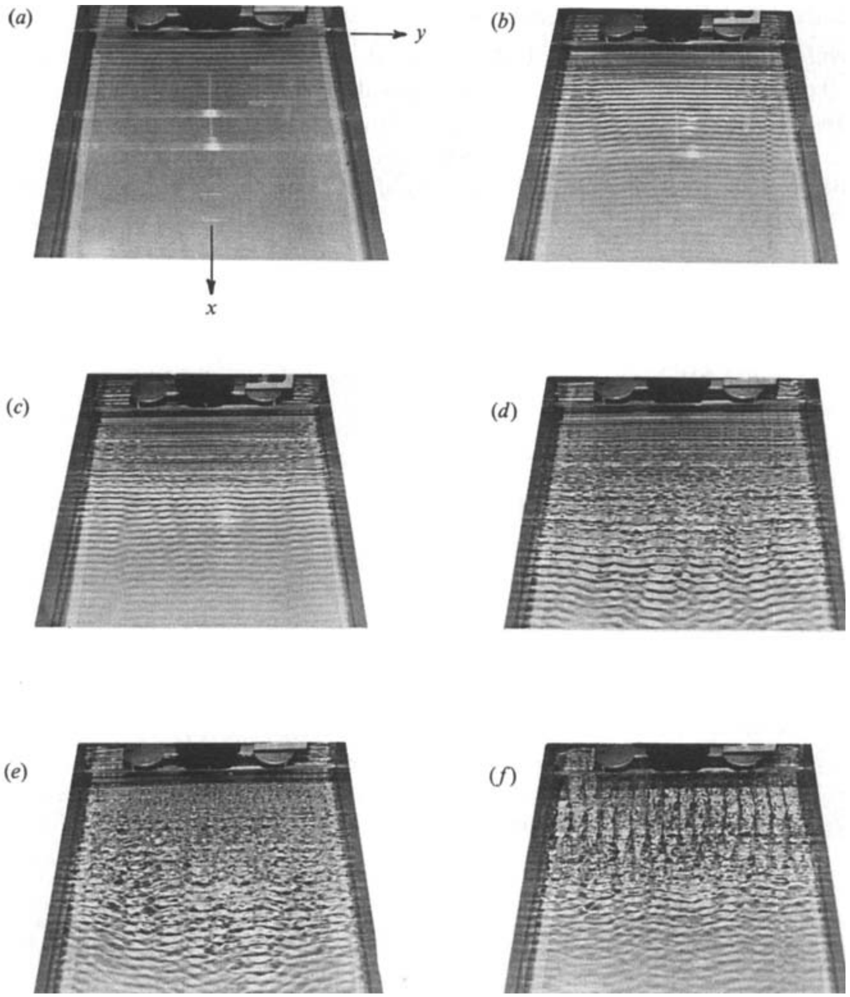

FIGURE 5. Overhead views showing spatial evolution of a 25 Hz wavetrain with increasing paddle stroke: $b = 30.5$ cm, $h = 4.9$ cm, $T = 73$ dyn/cm. (*a*) $sk_1 = 0.04$; (*b*) $sk_1 = 0.23$; (*c*) $sk_1 = 0.29$; (*d*) $sk_1 = 0.46$; (*e*) $sk_1 = 0.67$; (*f*) $sk_1 = 1.08$.

shown in figure 5. Each photograph presents an overhead view looking up the test channel toward the wavemaker; about 35 wavelengths of propagation are visible. (According to (2), $k_1 = 6.325\ \text{cm}^{-1}$ and the wavelength $L_1 = 2\pi/k_1 = 0.99$ cm for the 25 Hz wavetrain.) The vertical amplitude of the wavemaker stroke s is varied so that the product sk_1 varies from 0.04 in figure 5(*a*) to 1.08 in figure 5(*f*). The parameter sk_1 may be considered a measure of nonlinearity in the generation process which is related to the steepness $a_1 k_1$ of the progressing test wave. (Nonlinearity in the progressing waves for each of these experiments will be discussed shortly.) Wave crests remain straight and uniform in amplitude for the experiment with the smallest stroke shown in figure 5(*a*); there is no visible evidence of instabilities. As nonlinearity is increased in figure 5(*b*), the first few waves appear uniform in amplitude, but striations then appear on the surface at slight angles to the channel axis. These striations represent depressions in crest amplitude and the manifestation of two-

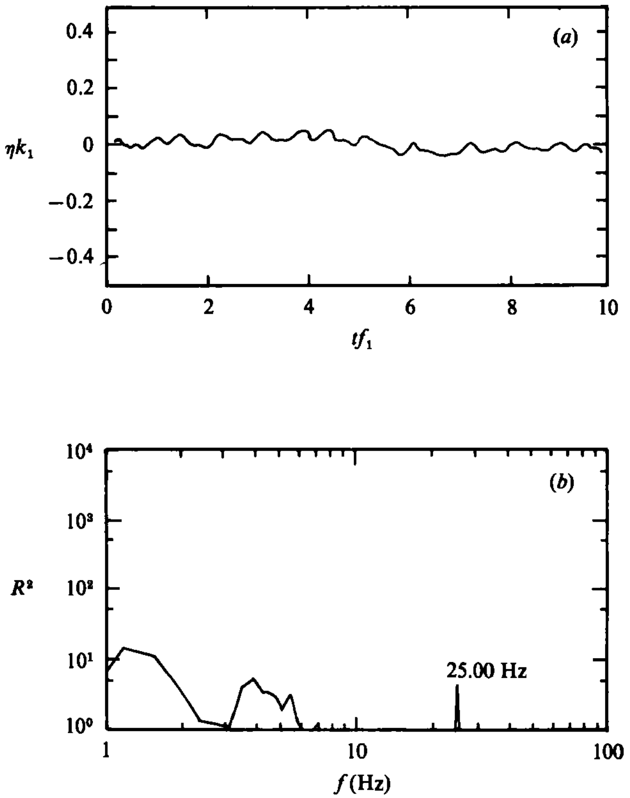

FIGURE 6. Temporal measurements of the 25 Hz wavetrain shown in figure 5(*a*): $sk_1 = 0.04$, $x = 7L_1$, $y = -4.8L_1$. (*a*) wave profile, (*b*) periodogram.

dimensionality in the wave pattern. Striations increase in number as nonlinearity increases until the water surface becomes very 'disordered' in figure 5(*d*). (Here we use the word 'disorder' to indicate that a wide variety of lengthscales appear to be present in the water surface pattern.) Note that the disorder is confined to a region of finite extent beginning a few wavelengths from the paddle and declining after about twenty wavelengths. Henceforth, the wave pattern becomes more ordered; i.e. fewer lengthscales appear to be present, though the waves remain short-crested. In this final stage of evolution the waves appear to experience rapid changes in phase across the striations as indicated by the offset of light and dark bands in the photographs. A hexagonal surface pattern develops which appears quite stable maintaining its form until extinguished by viscosity. (The hexagonal pattern of wave crests is not clearly visible in figure 5.) The further increase in nonlinearity shown in figure 5(*e*) leads to more intense disorder as evidenced by the finer spatial scales that appear to be present. The disordered region again is confined to a finite extent downstream as in figure 5(*d*). Finally, an entirely different wavefield is generated in the most nonlinear experiment of figure 5(*f*) where (subharmonic) cross-waves form at the paddle. The crests of these cross-waves are normal to the paddle and remain distinct for at least ten wavelengths downstream. We return to a discussion of cross-waves in §4.5.

The photographs of figure 5(*a–e*) suggest that the evolution of ripple wavetrains from generation to near extinction by viscosity can be divided conveniently into three regions, when cross-waves are not present. Region I consists of straight- and

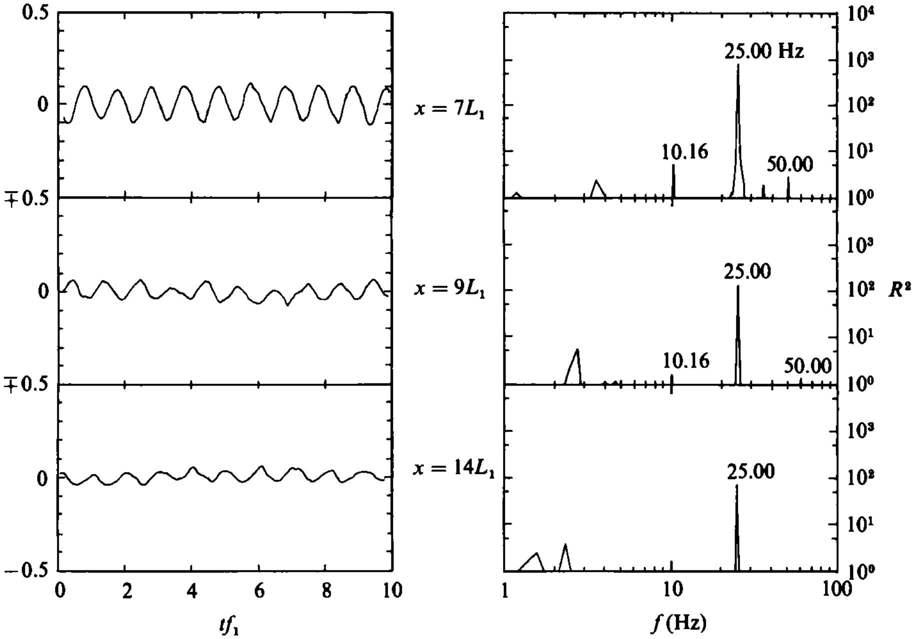

FIGURE 7. Temporal wave profiles and corresponding periodograms for the 25 Hz wavetrain of figure 5(b): $sk_1 = 0.23$, $y = -4.8L_1$.

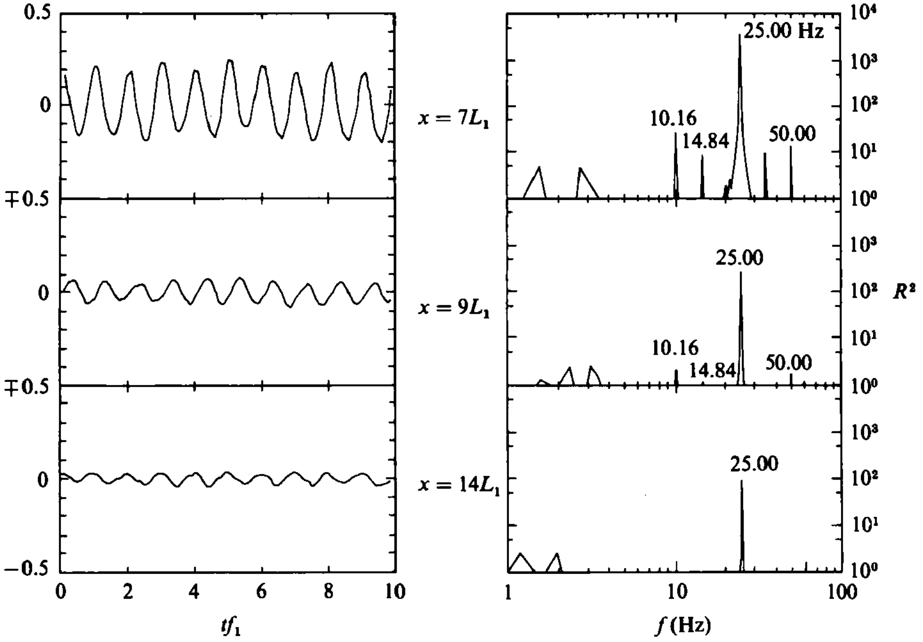

FIGURE 8. Temporal wave profiles and corresponding periodograms for the 25 Hz wavetrain of figure 5(c): $sk_1 = 0.29$, $y = -4.8L_1$.

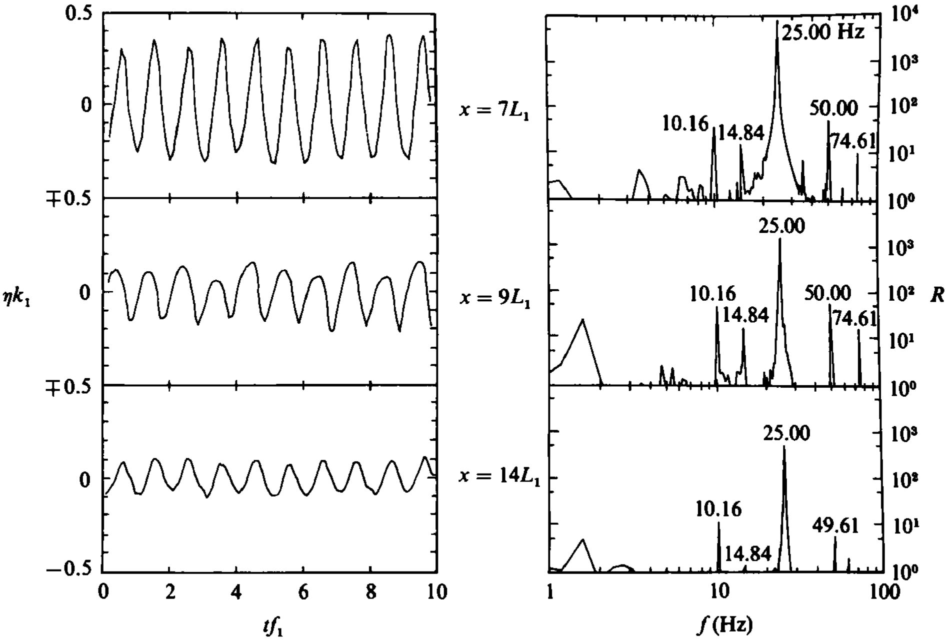

FIGURE 9. Temporal wave profiles and corresponding periodograms for the 25 Hz wavetrain of figure 5(*d*): $sk_1 = 0.46$, $y = -4.8L_1$.

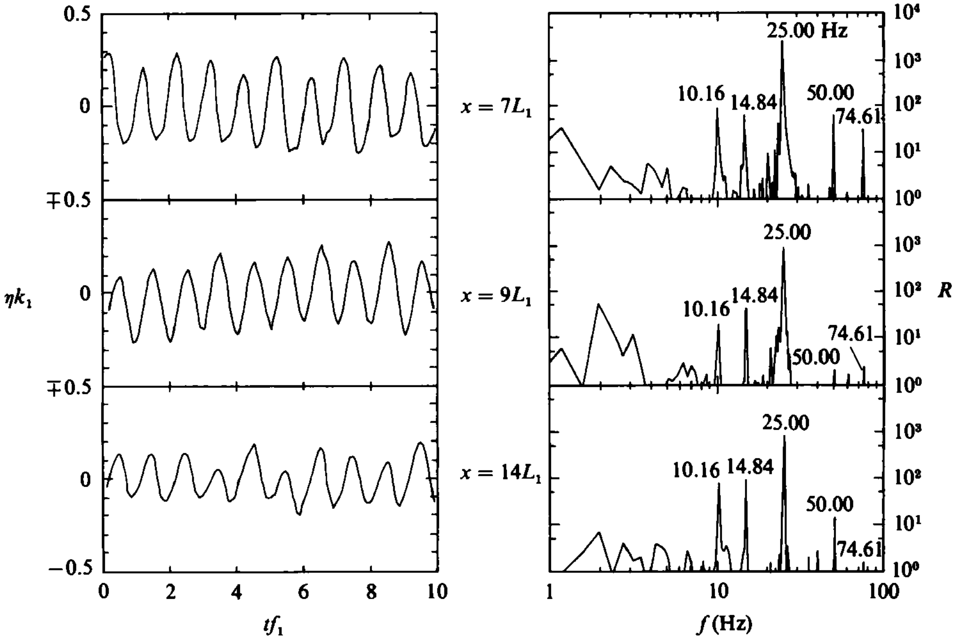

FIGURE 10. Temporal wave profiles and corresponding periodograms for the 25 Hz wavetrain of figure 5(*e*): $sk_1 = 0.67$, $y = -4.8L_1$.

uniform-crested waves beginning at the wavemaker. For small values of sk_1 this region appears to persist until the waves are annihilated by viscosity. For moderate values of sk_1, all three regions exist. They consist of Region I which is limited to a few wavelengths from the paddle, followed by Region II where the wave pattern is two-dimensional and characterized by striations and/or disorder, followed by Region III where the wave pattern becomes more ordered (only weakly two-dimensional) before being extinguished by viscosity. For strong nonlinearity in the generation process, cross-waves occur and dominate the observed wavefield. Region II appears to be the consequence of resonant triad interactions, evolving from nascent perturbations in Region I, and is of primary interest in this study. The temporal wave data presented below are obtained in Region II.

4.1.2. *Temporal data*

Before examining the temporal wavefields of figure 5 for moderate nonlinearity in the generation process, it is instructive to examine the experiment of figure 5 (*a*) where nonlinearity is very small. (Recall that the spatial data of figure 5 (*a*) do not show the presence of any instabilities.) Figure 6 presents a temporal wave profile ηk_1 and its corresponding periodogram obtained at $x = 7L_1$ and $y = -4.8L_1$ (to the left of the channel centreline as viewed in figure 5). Even though the spatial view of figure 5 (*a*) looks quite regular, the temporal record of figure 6 (*a*) shows that the 25 Hz wave is quite distorted. The periodogram of figure 6 (*b*) shows energy at low (noise) frequencies comparable in strength to the distinct spike at 25.00 Hz of the generated wave. Even though the wave profile is irregular, there is no evidence of any resonance phenomenon in the energy spectrum of this experiment. Data obtained beyond $x = 7L_1$ show that the energy of the 25.00 Hz wave continually decreases relative to that at low frequencies.

The absence of resonant interactions in the 25 Hz wavetrain of figures 5 (*a*) and 6 is not surprising when the small amplitude of the generated waves is considered. After seven wavelengths of propagation, figure 6 (*a*) indicates an approximate amplitude of $a_1 k_1 = 0.02$ or $a_1 = 0.03$ mm for the wavetrain. According to (11), the minimum threshold amplitude for resonant triad growth is $a_1 = 0.10$ mm; hence, no triads should occur.

Figures 7–10 present temporal wave profiles ηk_1 and corresponding periodograms for the experiments of moderate nonlinearity shown in figures 5 (*b–e*), respectively. In each case results are presented at three downstream locations $x = 7L_1$, $9L_1$, and $14L_1$ with $y = -4.8L_1$ as before. Recall that the generation nonlinearity sk_1 increases in this sequence of experiments. The nonlinearity $a_1 k_1$ in the progressing wave for each experiment is easily estimated from the wave profile at $x = 7L_1$. Wave steepness increases from $a_1 k_1 = 0.10$ in figure 7 to $a_1 k_1 = 0.35$ in figure 9, then, surprisingly, decreases to about $a_1 k_1 = 0.20$ in figure 10. The decrease in steepness of the test wave in figure 10 resulting from an increased wavemaker stroke and the large steepness of the previous experiment suggest that wave breaking might be occurring, although none was observed. Alternatively, more energy in the test wave may be transferring to other waves through resonant interactions. (Comparisons of the wave profiles and periodograms at $x = 7L_1$ in figures 8 and 10 offer some support for the latter alternative. We return to discuss resonant interactions momentarily.) The temporal wave profiles in figures 7–10 show significant decay in the amplitude of the test wave from $x = 7L_1$ to $x = 14L_1$. The amount of energy lost during propagation cannot be explained solely in terms of viscous damping. The *e*-folding distance U_1/δ_1 for viscous damping of a 25 Hz test-wave is about 11 wavelengths (see §2). Hence, the amplitude

Figure	Wavemaker frequency (Hz)	Test wave						Excited triad waves			
		f_1 (Hz)	L_1 (cm)	k_1 (cm^{-1})	sk_1	x/L_1	y/L_1	f (Hz)	k (cm^{-1})	l (cm^{-1})	m (cm^{-1})
12(*a*)	22.00	21.88	1.11	5.67	0.61	14.0	0	5.86	1.24	1.24	0
								16.02	4.32	4.32	0
11(*a*)	25.00	25.00	0.99	6.33	0.57	14.0	−4.8	10.16	2.70	2.46	1.11
								14.84	4.02	3.87	−1.11
12(*b*)	27.00	26.95	0.94	6.71	0.59	14.0	0	6.25	1.38	1.31	0.42
								20.70	5.42	5.40	−0.42
13(*a*)	30.00	30.08	0.86	7.31	0.58	10.0	−5.5	none	—	—	—
13(*b*)	32.00	32.03	0.82	7.67	0.56	10.0	−5.8	none	—	—	—
12(*c*)	34.00	33.98	0.78	8.02	0.68	8.7	−6.1	7.81	1.93	1.56	1.13
								26.17	6.56	6.46	−1.13
12(*d*)	36.00	35.94	0.75	8.37	0.77	14.0	0	11.72	3.17	2.51	1.93
								24.22	6.17	5.86	−1.93
12(*e*)	37.99	37.89	0.72	8.70	0.78	9.4	−6.6	15.63	4.23	3.47	2.41
								22.27	5.76	5.23	−2.41
12(*f*)	40.00	39.84	0.70	9.03	0.74	9.9	−6.9	19.92	5.24	4.52	2.66
								19.92	5.24	4.52	−2.66
12(*g*)	44.00	43.75	0.65	9.67	0.61	10.5	0	16.41	4.42	3.46	2.75
								27.34	6.79	6.21	−2.75
12(*h*)	46.01	45.70	0.63	9.99	0.54	10.8	−7.6	14.45	3.92	2.87	2.67
								31.64	7.60	7.12	−2.67

TABLE 1. Summary of experimental parameters and results for eleven experiments in the triad frequency range. Frequencies f_1 are measured from periodograms in the indicated figures; wavevectors $\boldsymbol{k} = (l, m)$ are calculated from the linear dispersion relation.

$a_1 k_1 = 0.10$ at $x = 7L_1$ in figure 7 is expected to decay to $a_1 k_1 = 0.05$ at $x = 14L_1$. Instead, the downstream wave experiences much more decay; its steepness is $a_1 k_1 = 0.02$. A similar result is obtained for each of the other test waves in figures 8–10. The portion of energy lost from the test waves during propagation, unaccounted for by viscous damping, may be due to energy transfer to other waves through resonant and other nonlinear interactions.

All of the periodograms in figures 7–10 indicate a remarkably simple result: as the 25.00 Hz wave propagates it excites two waves with frequencies of 10.16 and 14.84 Hz. Using (2) or simply noting the band of admissible frequencies for triads in figure 2, it is easily shown that the kinematical constraint on wavevectors in (3) is satisfied by these three waves. (The components of the wavevectors $\boldsymbol{k} = (l, m)$ for each triad member are listed in table 1.) Hence, there appears to be a selection process which results in a single resonant triad dominating evolution. Further examination of figures 7–10 indicates the following behaviour. The 10.16 Hz wave appears after seven wavelengths of the test-wave propagation in all experiments. This wave evolves faster than the 14.84 Hz wave and always contains more energy, except at one measurement station in the most nonlinear experiment (as regards generation) of figure 10. Only the 10.16 Hz wave occurs in the weakest nonlinear experiment of figure 7, and it is imperceptible in the periodogram at $x = 14L_1$ (presumably due to viscous attenuation). Both waves evolve in figure 8 but then disappear at the last station of measurement. The faster evolution of the lowest-frequency wave may result, at least in part, from the decrease in viscous effects with decreasing frequency as seen from (10). Of course, the inviscid rates of energy transfer among triad members are also a factor. In the more nonlinear experiments of figures 9 and 10 there is evidence of other waves being excited, presumably through non-resonant and other resonant interactions. In particular, narrow-band interactions occur about the test-wave and triad-member frequencies. (These narrow-band interactions are a consequence of higher-order nonlinear effects.) Among them is side-band growth reminiscent of the well-known Benjamin–Feir instability for deep-water gravity waves (e.g. see Lake *et al.* 1977). None of the other interactions is as pronounced as that of the resonant triad in which the 10.16 and 14.16 Hz waves are excited. At frequencies greater than 25 Hz, where triad interactions are not admissible, energy is observed at the 50.00 and 74.61 Hz superharmonics of the test wave. These superharmonics are generated directly by the wavemaker and by nonlinearity in the test wave. (A periodogram of the actual paddle motion shows similar superharmonics.) Note also that the wavemaker frequency (25.00 Hz) is equal to that resolved by the FFT calculations. Hence, no Doppler shifts by currents are apparent. It should also be mentioned that energy occurs at the known (see §3.2) and distinct 'noise' frequencies of 35.16, 60.16 and 92.19 Hz throughout the experiments of figures 7–10.

There are two experimental points noted in §3.1 which should be emphasized here. First, all temporal results are obtained using the gauge calibration of the test wave. Hence, the amplitudes and energy densities of lower-frequency waves are exaggerated; those of higher-frequency waves are attenuated. Secondly, only one gauge is used to obtain data; the gauge position is fixed and sk_1 of the generation process is varied. Hence, each of the downstream measurements actually represents a different experiment. The persistence in growth of the same resonant triad in differing experiments reflects the reproducibility of experiments and the robustness of the selection process.

4.1.3. *Effect of channel breadth*

For any water surface of finite extent the boundaries necessarily limit the possible wave modes to a countable set. In the ripple experiments reported herein the endwalls behind and in front of the paddle have negligible effect. The waves behind the paddle are very small *ab initio*, while the waves in front decay before striking the downstream wall (located 152 cm from the paddle). However, the temporary sidewalls used in the above experiments do reflect wave energy and limit the background waves with wavevectors at angles to the channel axis (transverse modes) to a countable set. In order to determine if these temporary walls affect the triad selection process, periodograms of two additional experiments are presented in figure 11. In both cases the temporal data are obtained at $x = 14L_1$ and $y = 0$. The experiment of figure 11 (*a*) utilizes the temporary sidewalls as before to form a channel of breadth $b = 30.5$ cm, and again shows the selection of the 25.00, 10.16, and 14.84 Hz triad. Figure 11 (*b*) shows a periodogram for the same experiment when the temporary sidewalls are removed. In this experiment the wavemaker paddle, with a length of 30.4 cm, oscillates astride the centreline of the tank's long axis paralleled by sidewalls which are 91 cm apart. The larger spacing between sidewalls provides a denser set of allowable transverse modes. Again, the 25.00, 10.16, and 14.84 Hz triad is selected; hence, the channel breadth of 30.5 cm appears to have an immeasurable effect on the triad selection process.

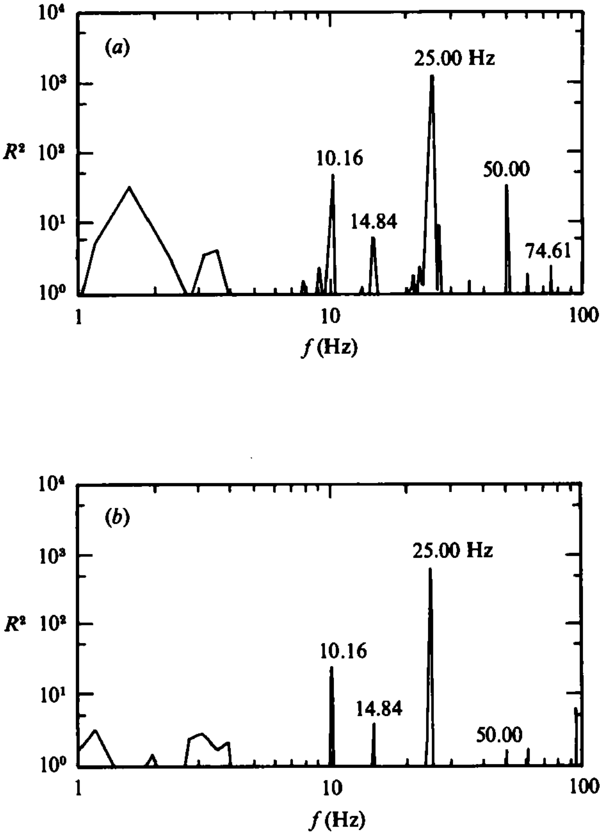

FIGURE 11. Periodograms for a 25 Hz wavetrain: $sk_1 = 0.57$, $x = 14L_1$, $y = 0$. (*a*) $b = 30.5$ cm, (*b*) $b = 91.0$ cm.

4.2. *Other wavetrains with frequencies greater than 19.6 Hz*

In order to determine if the selection process apparent for the 25 Hz wavetrain persists at other frequencies, we now examine a variety of test waves in the triad regime (> 19.6 Hz). For brevity, only a single periodogram is presented for each test-wave. Though we have chosen to present the periodogram for each experiment which best illustrates wave evolution, the observed behaviour is found in all data. Table 1 summarizes the results obtained from the periodogram of the indicated figure and the generation parameters for each experiment. Included among the latter are the wavemaker frequency, the test-wave frequency f_1 (resolved by the periodogram), k_1, sk_1, and the (x, y)-location of wave measurement. The channel breadth is 30.5 cm for all experiments.

Figure 12 shows periodograms for 8 test waves in the frequency range of 22–46 Hz. Careful examination of the periodograms indicates that a triad of waves is excited by each test-wave. Both the frequencies and wavevector components (l, m) of each triad are presented in table 1. All of the observed triads satisfy the resonance conditions of (3); hence, a selection process exists for each of the experiments in figure 12.

In the experiment of figure 12(*a*), the 5.86 Hz wave excited by the 21.88 Hz test-wave is just outside the band of admissible triad frequencies (see figure 2). Hence, the wavevector components do not satisfy precisely the resonance condition of (3).

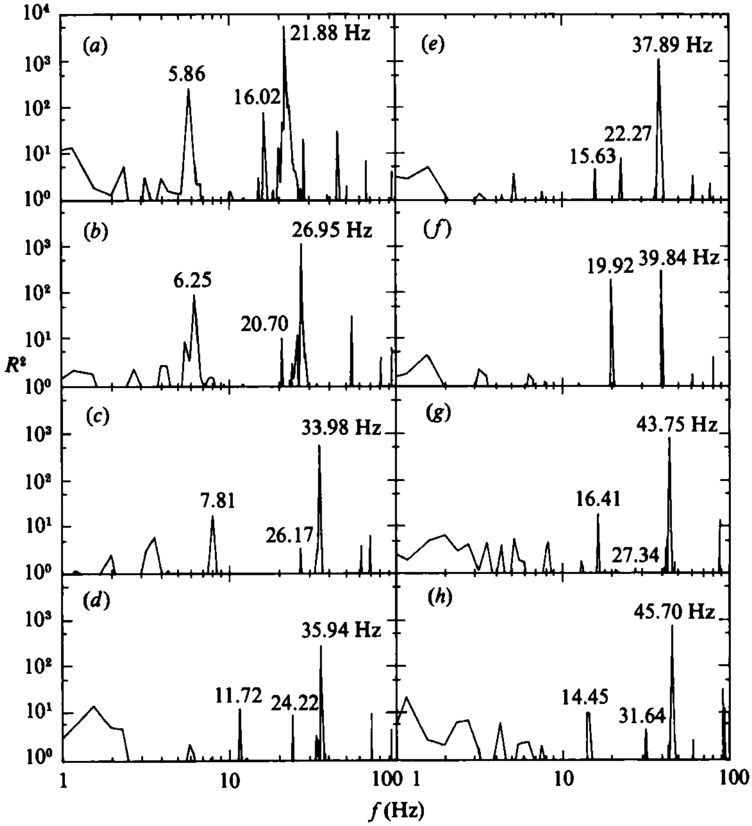

FIGURE 12. Periodograms for 8 wavetrains with $b = 30.5$ cm. Generation parameters and results are presented in table 1.

(Even here the error is less than 2%.) This small discrepancy is most likely the consequence of the poor resolution (±0.39 Hz) of low-frequency signals in the periodogram calculations. The 6.25 Hz wave excited by the 26.95 Hz test-wave in figure 12(*b*) is also very near (and within) the low-frequency boundary of the admissible triad band. Thus, the wavevectors in the resonant triads for both the 21.88 and 26.95 Hz test-waves are nearly collinear. Since viscous damping is smallest for the lowest-frequency member in the band of admissible triads, a selection mechanism related to viscosity might be postulated for these two experiments. However, the excited waves in all of the other experiments lie well within the admissible range, and wavevectors are not collinear. The 39.84 Hz wave of figure 12(*f*) is unique among the experiments exciting waves at its subharmonic frequency of 19.92 Hz. We emphasize here that after careful observation of the wavefield near the paddle we found no evidence of subharmonic cross-waves in this experiment. All of the excited waves listed in table 1 are very pronounced except for the 27.34 Hz wave excited by the 43.75 Hz wavetrain in figure 12(*g*). Although an energy peak was always found at 27.34 Hz, we were unable to measure energy levels comparable to that of the 16.41 Hz wave.

There are three additional aspects of the experiments in figure 12 which should be noted. First, similar to the behaviour of the 25 Hz test-wave, the lowest-frequency member of the resonant triad always evolves first, and generally maintains more energy than the other excited wave until both are no longer detectable. Second, the test-wave frequencies resolved by the periodograms are nearly equal to the wavemaker frequencies. (Differences are within the known resolution error of the FFT calculations.) Hence, currents are not a significant factor in the experiments. Third, many of the excited waves in figure 12 have frequencies in the triad regime. Presumably, these waves can also excite resonant triads; however, there is no experimental evidence that a pyramiding of triads is occurring. The absence of subsequent triads is probably a consequence of viscous effects. For example, the 24.22 Hz wave excited by the test wave in figure 12(*d*) has an amplitude of approximately 0.06 mm. (This amplitude is estimated from the relative energy densities and known amplitude of the test wave. Recall that the energy densities of low-frequency waves are exaggerated by the wave gauge; hence, 0.06 mm represents an upper bound.) According to (11), the minimum threshold amplitude required for the 24.22 Hz wave to excite a triad is about 0.10 mm. Therefore, subsequent triads are not expected in figure 12(*d*). A similar result is found for other excited waves with frequencies greater than 19.6 Hz in figure 12.

In the nine experiments presented till now, a selection process is clearly evident, and the selected triad persists over a wide range of amplitudes in the initial wave. In addition to these experiments, we have encountered two test waves for which no selection process is apparent. Figure 13 presents typical periodograms for 30.08 and 32.03 Hz test-waves obtained in a channel; generation parameters are summarized in table 1. In both periodograms, no waves in the admissible triad band appear to be excited. In fact, no significant amount of energy appears in these bands. Energy occurs primarily at noise frequencies, superharmonics, and in a narrow band of frequencies centred about that of the test wave. We emphasize that the results in figure 13 persist regardless of the amplitude of the initial wave or the measurement site.

4.3. *The 19.6 Hz and 9.8 Hz wavetrains*

In addition to waves in the triad regime of frequencies, it is also of interest to examine waves at the parametric boundary of 19.6 Hz for this regime and the degenerate case of triad resonance at 9.8 Hz, i.e. Wilton's ripples. Figure 14 shows wave profiles at $x = 5L_1$, $10L_1$ and $15L_1$ and corresponding periodograms obtained along the channel ($b = 30.5$ cm) axis in an experiment with a wavemaker frequency of 19.60 Hz. The 19.53 Hz test-wave (as resolved by the periodogram) excites its subharmonic frequency at 9.77 Hz whose energy increases slightly during propagation. However, the excitation of waves in a narrow band about the test-wave is more pronounced. Since these narrow-band interactions are a higher-order effect, the excitation of a subharmonic triad is indeed weak. Note that the test-wave superharmonics at 39.45 Hz and 58.98 Hz remain distinctive over the ten wavelengths of propagation shown in figure 14.

Figure 15 shows downstream wave profiles and corresponding periodograms for Wilton's ripples, again obtained along the centreline of the 30.5 cm channel. (The wavemaker frequency is 9.80 Hz.) At $x = 5L_1$ the profile of the 9.77 Hz test-wave is quite distinctive showing the effect of significant energy at its 19.53, 29.30, 39.06, and 48.83 Hz superhamonics. During subsequent propagation, Wilton's ripples excite significant growth of waves in a band of nearby frequencies. These narrow-band interactions even appear about the 19.53 Hz superharmonic (which is also a 'free'

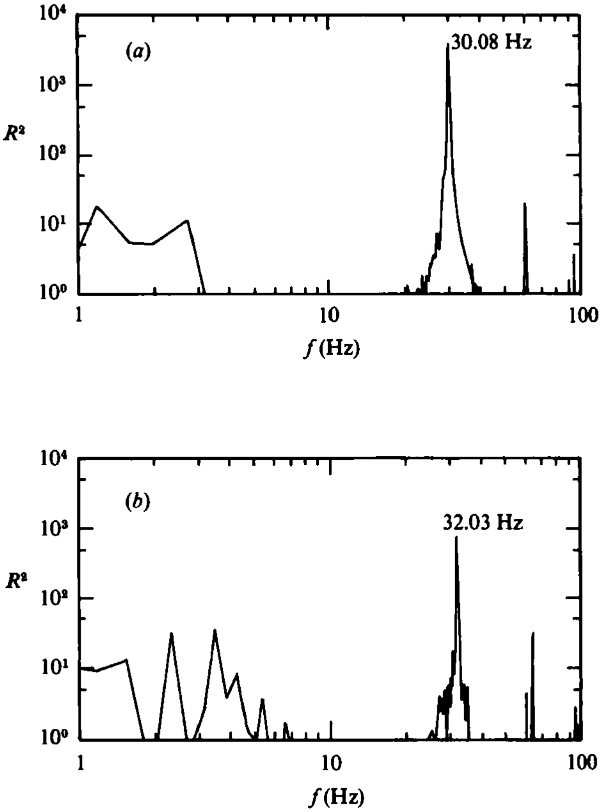

FIGURE 13. Periodograms for 2 wavetrains with $b = 30.5$ cm in which no dominant triad is selected. See table 1 for generation parameters.

wave) at the last measurement site. The proliferation of superharmonics in the data of figure 15 is dramatic evidence of the special instability of Wilton's ripples. Note that the 29.30 Hz superharmonic at $x = 10L_1$ contains even more energy than the 19.53 Hz superharmonic!

4.4. *Generation of subharmonic cross-waves*

When the generation parameter sk_1 is about one for the 25 Hz wave presented in §4.1, both subharmonic cross-waves and the test wave are generated as shown in the photograph of figure 5(f). The cross-waves have crests normal to the wavemaker paddle, and their amplitude decreases down the channel. In figure 5(f) they dominate the wavefield for at least 10 test-wave lengths from the paddle. Temporal wave profiles and periodograms at three measurement sites for the experiment of figure 5(f) are presented in figure 16. Even though a broad band of waves is excited, the subharmonic 12.11 Hz wave dominates each energy spectrum. The 25.00 Hz test-wave becomes more distinguished at downstream measurement sites. Note that even a sub-subharmonic wave with a frequency of 6.25 Hz is apparent at $x = 7L_1$.

Subharmonic cross-waves are the consequence of a strongly nonlinear instability known since Faraday (1831, as referenced by Rayleigh 1945, p. 347). These standing waves have been studied extensively in the context of gravity-wave generation (e.g.

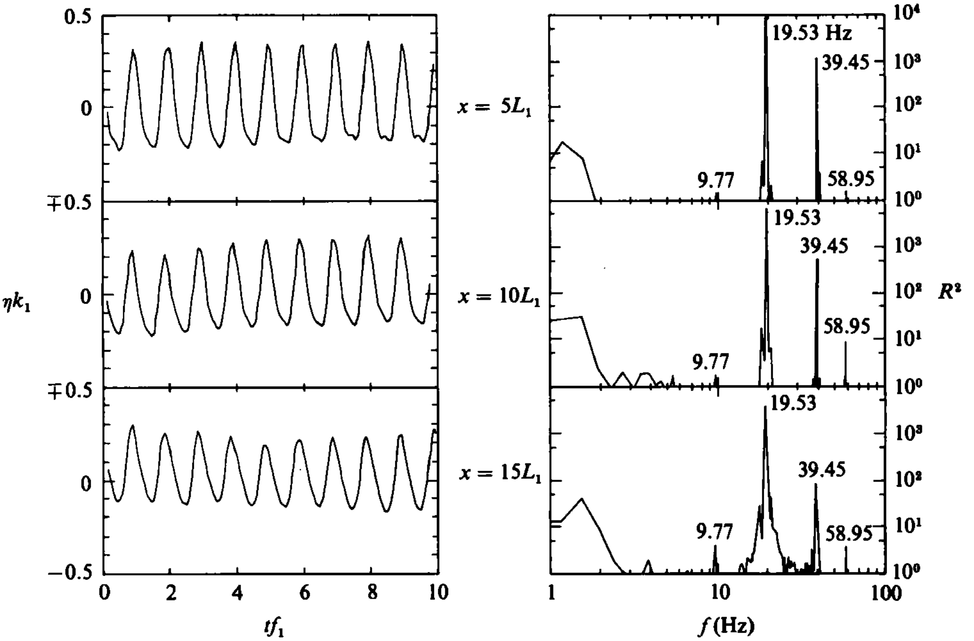

FIGURE 14. Temporal wave profiles and corresponding periodograms for a 19.6 Hz wavetrain: $sk_1 = 0.35$, $y = 0$.

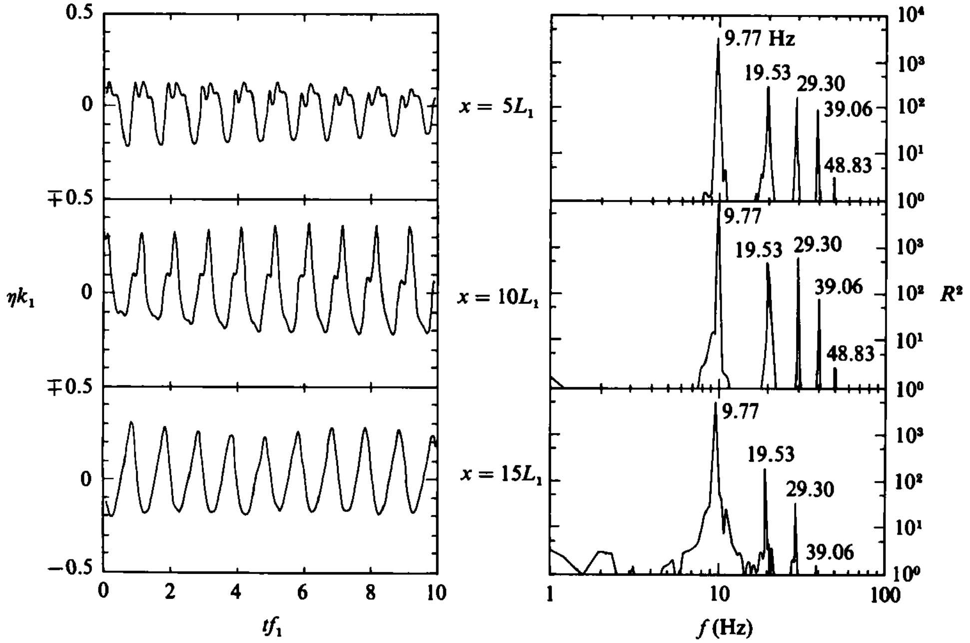

FIGURE 15. Temporal wave profiles and corresponding periodograms for Wilton's ripples (9.8 Hz): $sk_1 = 0.32$, $y = 0$.

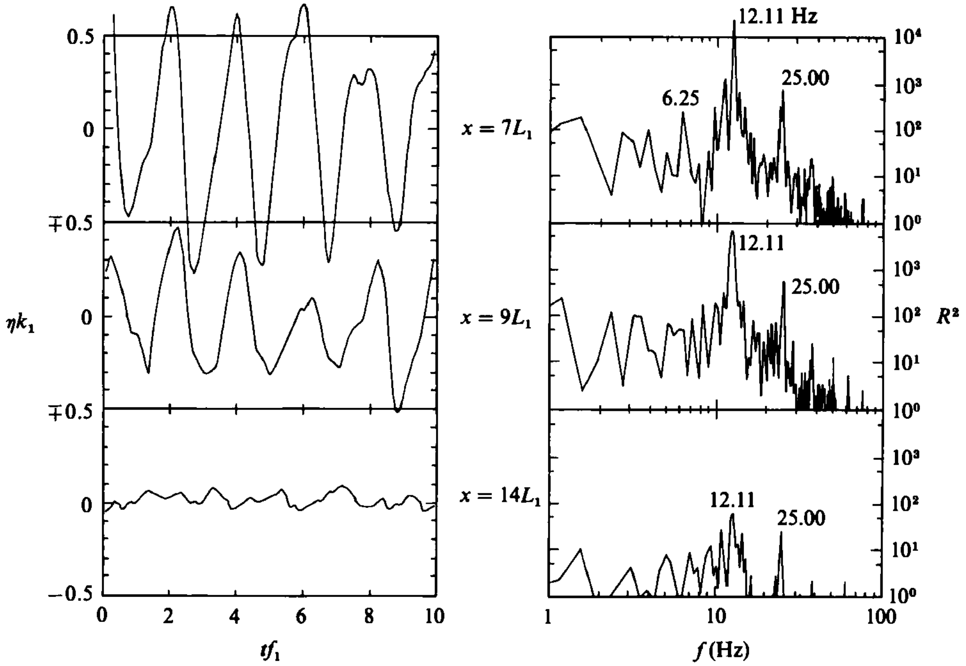

FIGURE 16. Temporal wave profiles and corresponding periodograms for the 25 Hz wavetrain of figure 5(f): $sk_1 = 1.08$, $y = -4.8L_1$.

see Lichter & Chen 1987 and the references they cite). The occurrence of cross-waves is stressed here because of their relative ease of generation and the resulting contamination of the weakly nonlinear, resonant triad interactions whose nature is under study. (We note that cross-waves at the frequency of the paddle oscillation are even easier to generate. However, these synchronous modes are much more localized, and less likely to contaminate downstream measurements.)

Contamination by subharmonic cross-waves is a possible explanation for the contradictory experimental results reported by Bannerjee & Korpel (1982, hereinafter referred to as BK). In a set of experiments similar to those reported here, BK find the consistent excitation of subharmonics which they attribute to weakly nonlinear, triad interactions. Their results directly contradict all but one of the present experiments, except when cross-waves are generated. (The single exception is the 39.84 Hz test-wave of figure 12(f). Recall that observations of the wavefield near the paddle during this experiment found no evidence of subharmonic cross-waves.) Although BK report no direct evidence of cross-wave generation, the following circumstantial evidence is noted. (i) BK used test-wave frequencies in the range of 30–100 Hz, and presented temporal and spatial data for a 60 Hz wave. BK did not report paddle strokes or wave steepness in their experiments; however, Hogan (1984) re-examined their data and suggested that the nonlinear effects on wave dispersion were significant. The high frequencies of their experiments and Hogen's analysis suggest that the waves in their experiments were very nonlinear. (ii) The measurements of BK were made within one test-wave length of the paddle where cross-waves surely dominate if present. (iii) The authors reported that subharmonic waves were most distinct when data were measured to the side of the paddle. Without sidewalls directly adjacent to the paddle, the progressive wave components forming the standing cross-waves on the paddle can propagate into lateral regions. Our experience is that it is difficult to measure any significant wave activity to the side of the paddle when no cross-waves are generated. (iv) BK indicate that the onset of the subharmonic occurred at a threshold amplitude. The only threshold involved in weakly nonlinear interactions is due to viscosity. It is extremely doubtful that the nonlinearity in the BK experiments was as small as that required for the viscous threshold to play a role. However, cross-waves are known to occur suddenly at a (large) threshold amplitude. All of these factors, when combined with the experimental data presented herein, suggest that the data of BK were contaminated by subharmonic cross–waves.

5. Summary and conclusions

The well-known instability of ripple wavetrains on deep water is reaffirmed by experiments in which waves are generated mechanically in a channel. Experiments are presented for eleven wavetrains with frequencies greater than 19.6 Hz where a continuum of resonant triad interactions are dynamically admissible. Results from these experiments are summarized in table 1. (Resonant triad interactions are theoretically impossible for waves with frequencies less than 19.6 Hz, except for the degenerate case of Wilton's ripples at 9.8 Hz.) Experimental data are also presented for the parametric wavetrain with a frequency of 19.6 Hz and Wilton's ripples at 9.8 Hz.

The spatial evolution of an unstable wavetrain from generation to near extinction by viscosity is similar among all experiments. For moderate nonlinearity in the generation process, the spatial evolution is conveniently divided into three behavioural regions. Region I is near the wavemaker paddle where crests are straight and (nearly) uniform in amplitude with only slight evidence of nascent perturbations. These perturbations grow in Region II until the surface wave pattern becomes distinctly two-dimensional. When nonlinearity is small, the two-dimensionality is characterized by striations at slight angles to the direction of wave propagation. These striations correspond to depressions in the amplitudes of wave crests. As nonlinearity increases the surface pattern becomes disordered; i.e. many lengthscales appear to be present. Beyond Region II the waves evolve into a more ordered pattern which is only weakly two-dimensional. The weakly two-dimensional pattern of Region III is also characterized by striations at slight angles to the dominant direction of wave propagation. The wave phases experience rapid changes across these striations leading to a hexagonal wave pattern. The hexagonal waves appear to be very stable, persisting in form until they are annihilated by viscosity. For weak-generation nonlinearity, only Region I occurs before the waves are extinguished by viscosity. For strong-generation nonlinearity, subharmonic and synchronous cross-waves occur; the subharmonic waves completely dominate the wavefield for some distance from the wavemaker. The wave behaviour in Region II appears to be dominated by resonant triad interactions for most experiments, and all quantitative data are obtained in this region.

Even though the wave pattern in Region II can appear spatially disordered, quantitative temporal data indicate that the dominant process occurring there is quite ordered. In fact, for nine of the eleven test waves with frequencies greater than 19.6 Hz, a selection process exists in which a single, resonant triad is excited from the available continuum. The selection process is very robust, persisting for amplitudes ranging from the (small) threshold value needed to overcome viscous damping to the (large) value resulting in cross-wave generation. The presence of a selection process is not evident in the form of the interaction coefficients of the three-wave equations or the initial growth–decay rate governing the evolution of an isolated ripple triad. These parameters exhibit extrema for near-subharmonic triads but vary smoothly over a band of allowable frequencies. In the nine experiments exhibiting selection, the subharmonic resonant triad occurs only once. No pattern is apparent in the frequencies of waves selected in the other experiments. The absence of a pattern suggests that viscosity is not important in selection, since damping of wavetrains is frequency dependent. For two of the eleven test waves no selection process is evident; only narrow-band interactions are detectable. No explanation is offered for either the presence or absence of a triad selection process. Presumably, both forms of behaviour are present in solutions of the three-wave equations, though no calculations are presented. Clearly, viscosity eventually annihilates all interactions, and may play a dominant role in the long-term evolution observed in Region III.

Although viscosity does not appear to be important in triad selection, it may be responsible for the following two observations. First, when a triad is selected, the lowest-frequency member always evolves first, and generally maintains more energy than the other excited wave until both are annihilated by viscosity. Secondly, excited waves in the first triad with frequencies greater than 19.6 Hz do not generate subsequent triads.

All of the experiments (with the single exception of Wilton's ripples) conform to Hasselmann's theorem; the test wave always has the highest frequency in the triad. In addition, surface currents do not appear to be significant in any experiment.

The 19.6 Hz wavetrain at the parametric boundary of the triad regime shows only weak excitation of its subharmonic. Narrow-band interactions dominate evolution with distinctive side-band growth reminiscent of the well-known Benjamin–Feir instability. The experiment for Wilton's ripples at 9.8 Hz shows prolific excitation of its superharmonics as well as narrow-band interactions.

Care is required in performing experiments on ripples and capillary waves to avoid the generation of synchronous and subharmonic cross-waves at the paddle. When subharmonic cross-waves occur, they dominate the wavefield for some distance down the channel, and completely obscure weakly nonlinear interactions such as the resonant triads examined here. Contamination of experimental data by subharmonic cross-waves is a possible explanation for the contradictory experimental results of BK. BK found consistent subharmonic excitation which they attributed to weakly nonlinear, resonant triad interactions. The subharmonic triad occurred in only one of our experiments when no subharmonic cross-waves were observed at the paddle.

The authors gratefully acknowledge many helpful comments from Harvey Segur, John Scott, Jerry Gollub and the Journal referees. Special gratitude is also owed to the Office of Naval Research, Fluid Dynamics Program for patience and financial support under contracts N00014-82-K-0641 and N00014-86-K-0097 with the University of Florida. D.M.H would also like to thank the Department of Engineering Sciences at the University of Florida and her advisor (J.L.H) for providing a stimulating environment in which to pursue graduate study.

REFERENCES

BANNERJEE, P. P. & KORPEL, A. 1982 Subharmonic generation by resonant three-wave interaction of deep-water capillary waves. *Phys. Fluids* **25**, 1938–1943.

BENNEY, D. J. 1962 Non-linear gravity wave interactions. *J. Fluid Mech.* **14**, 577–584.

BLOOMFIELD, P. 1976 *Fourier Analysis of Time Series: An Introduction.* John Wiley.

CRAIK, A. D. D. 1986 Exact solutions of non-conservative equations for three-wave and second harmonic resonance. *Proc. R. Soc. Lond.* A **406**, 1–12.

FARADAY, M. 1831 On the forms and states assumed by fluid in contact with vibrating elastic surfaces. *Phil. Trans. R. Soc.* **31**, 319.

HARRISON, W. J. 1909 The influence of viscosity and capillarity on waves of finite amplitude. *Proc. Lond. Math. Soc.* **7**, 107–121.

HASSELMANN, K. 1967 A criterion for nonlinear wave stability. *J. Fluid Mech.* **30**, 737–739.

HENDERSON, D. M. & LEE, R. C. 1986 Laboratory generation and propagation of ripples. *Phys. Fluids* **29**, 619–624.

HOGAN, S. J. 1984 Subharmonic generation of deep-water capillary waves. *Phys. Fluids* **27**, 42–45.

KAUP, D. J. 1981 The solution of the general initial value problem for the full three dimensional three-wave resonant interaction. *Physica* **3D** 1 and 2, 374–395.

LAKE, B. M., YUEN, H. C., RUNGALDIER, H. & FERGUSON, W. E. 1977 Nonlinear deep-water waves: theory and experiment. Part 2. Evolution of a continuous wave train. *J. Fluid Mech.* **83**, 49–74.

LAMB, H. L. 1895 *Hydrodynamics*, 2nd edn. Cambridge University Press.

LAMB, H. L. 1932 *Hydrodynamics*. Dover Publication.

LICHTER, S. & CHEN, J. 1987 Subharmonic resonance of nonlinear cross-waves. *J. Fluid Mech.* **183**, 451–465.

LUCASSEN-REYNDERS, E. H. & LUCASSEN, J. 1969 Properties of capillary waves. *Adv. Colloid Interface Sci.* **2**, 347–395.

MCGOLDRICK, L. F. 1965 Resonant interactions among capillary–gravity waves. *J. Fluid Mech.* **21**, 305–331.

MCGOLDRICK, L. F. 1970 An experiment on second-order capillary gravity resonant wave interactions. *J. Fluid Mech.* **40**, 251–271.

PHILLIPS, O. M. 1960 On the dynamics of unsteady gravity waves of finite amplitude. Part 1. The elementary interactions. *J. Fluid Mech.* **9**, 193–217.

RAYLEIGH, LORD 1890 On the tension of water surfaces, clean and contaminated, investigated by the method of ripples. Reprinted 1964 in *Scientific Papers*, vol. 3, pp. 397–425. Dover.

RAYLEIGH, LORD 1945 *The Theory of Sound.* Dover.

SCOTT, J. C. 1979 The preparation of clean water surfaces for fluid mechanics. In *Surface Contamination: Genesis, Detection and Control*, vol. 1 (ed. K. L. Mittal), pp. 477–497. Plenum.

SIMMONS, W. F. 1969 A variational method for weak resonant wave interactions. *Proc. R. Soc. Lond.* A **309**, 551–575.

STOKES, G. G. 1847 On the theory of oscillatory waves. *Trans. Camb. Phil. Soc.* **8**, 441–455.

WILTON, J. R. 1915 On ripples. *Phil. Mag.* **29** (6), 688–700.